Quantum Interference and Optical Tuning of Self-Trapped Exciton State in Double Halide Perovskite

Kai-Xuan Xu(徐开轩)[1,2†], Xin-Bao Liu(刘新豹)[3,7†], Simin Pang(庞思敏)[1,2†], Zhe Zhang(张哲)[1,2], Yubin Wang(王毓彬)[5], Haonan Chang(常浩男)[1,2], Jiajun Luo(罗家俊)[6], Jiang Tang(唐江)[6], Qihua Xiong(熊启华)[5], Sheng Meng(孟胜)[3,7*], Shiwu Gao(高世武)[4*], and Jun Zhang(张俊)[1,2*]

[1]*State Key Laboratory of Semiconductor Physics and Chip Technologies, Institute of Semiconductors, Chinese Academy of Sciences, Beijing 100083, China*
[2]*Center of Materials Science and Optoelectronics Engineering, University of Chinese Academy of Sciences, Beijing 100049, China*
[3]*Beijing National Laboratory for Condensed Matter Physics, Institute of Physics, Chinese Academy of Sciences, Beijing 100190, China*
[4]*Beijing Computational Science Research Center, Beijing 100193, China*
[5]*State Key Laboratory of Low-Dimensional Quantum Physics and Department of Physics, Tsinghua University, Beijing 100084, China*
[6]*Wuhan National Laboratory for Optoelectronics (WNLO), School of Optical and Electronic Information, Huazhong University of Science and Technology (HUST), Wuhan 430074, China*
[7]*School of Physical Sciences, University of Chinese Academy of Sciences, Beijing 100190, China*

(Received 8 December 2025; accepted manuscript online 13 January 2026)

Self-trapped excitons (STEs), known for their unique radiative properties, have been harnessed in diverse photonic devices; however, their comprehensive understanding and manipulation remain elusive. In this study, we present novel experimental and theoretical evidence revealing the hybrid nature and optical tunability of STE state in $Cs_2Ag_{0.4}Na_{0.6}InCl_6$. The detection of the Fano resonance in laser energy-dependent Raman and photoluminescence spectra indicates the emergence of an exciton-phonon hybrid state, arising from robust quantum interference between the discrete phonon and continuum exciton states. Moreover, we demonstrate continuous tuning of this hybrid state with the energy and intensity of the laser field. These findings lay the foundation for a comprehensive understanding of the nature of STE and their potential for state control.

DOI: 10.1088/0256-307X/43/3/030703 CSTR: 32039.14.0256-307X.43.3.030703

1. Introduction. Electron–phonon coupling significantly affects the electrical conductivity,[1,2] superconductivity,[3] and optical absorption properties of materials.[2,4] A prominent example of electron-phonon coupling in condensed matter is the polaron, a quasiparticle comprising an electron (hole) and the lattice distortion it induces. Polarons can be categorized into large and small polarons based on their radius of spatial extension, depending on the effective mass of the carrier and the dielectric environment.[5,6] When the electron-phonon coupling is sufficiently strong, small polarons tend to be localized in a specific region. In this case, the electron propagates with a local lattice distortion, resembling being "dressed" by phonons, which affects its effective mass and mobility.[7,8] Polarons are crucial for understanding charge transport[9] and optical emission in materials,[10] such as semiconductors,[11] oxides,[6] and ionic crystals.[12] For neutral excitons, when the electron-phonon and hole-phonon couplings vary such that they cannot cancel each other, the spatial charge fluctuations of electrons and holes can induce lattice distortions. This crucial difference originates from a pronounced mismatch in their deformation potentials ($|D_e - D_h|$), which quantifies the energy shift per unit lattice strain. Such a mismatch emerges directly from the spatially separated and orbitally distinct nature of the electron and hole, a hallmark of charge-transfer exciton self-trapping.[13,14] This condition leads to strong exciton-phonon couplings, where the distortions bind the exciton[15] to form a self-trapped exciton (STE), called an exciton polaron. This stable state influences radiative recombination[16,17] in a manner analogous to that of polaron formation. Owing to their large lattice displacements, STE materials can produce broadband luminescence with an extremely high photoluminescence quantum yield (PLQY), making them ideal for high-efficiency lasers[18] and white-light emitters.[16,19] Therefore, understanding the mechanisms of self-trapping and the manipulation of these states is essential for targeted applications.

†These authors contributed equally to this work.
*Corresponding authors. Email: smeng@iphy.ac.cn; swgao@csrc.ac.cn; zhangjwill@semi.ac.cn
© 2026 Chinese Physical Society and IOP Publishing Ltd. All rights, including for text and data mining, AI training, and similar technologies, are reserved.

The essence of exciton-phonon coupling in STEs lies in the formation of a hybrid quasiparticle, wherein the exciton is strongly coupled to vibronic phonons. This coupling induces the exciton to be "dressed" by a cloud of phonons, forming a hybrid quantum state with both exciton and phonon characteristics. Despite extensive optical spectroscopy revealing electronic band reorganization[20,21] and lattice vibrations,[22,23] the precise nature and quantitative description of this hybrid STE state remain elusive. The hybrid state can be directly confirmed using resonant Raman and photoluminescence (PL) techniques, where the phonon frequency and STE energy are expected to exhibit resonance quantum interference. A notable example is the Fano resonance, emerging from the interference between discrete phonon and continuum exciton states, providing unique insights into strongly interacting physics,[2,24,25] including magnetization and electronic polarization,[26,27] resonant electromagnetic effects,[28] and exciton-phonon interactions.[29–31] Specifically, the Fano resonance observed in Raman scattering owing to exciton-phonon interactions is a powerful tool for elucidating the underlying physics of solid materials.[2,30,31] Among the most promising STE materials, lead-free double perovskites[32] excel in their environmental friendliness and high stability, with potential applications in white-light sources,[33] photodetectors,[34] solar cells,[35] and X-ray detectors.[36]

In this study, we presented theoretical and experimental evidence elucidating the nature and formation dynamics of an exciton-phonon hybrid STE state in the double-halide perovskite $Cs_2Ag_{0.4}Na_{0.6}InCl_6$ and demonstrated the effective modulation of the STE state using a steady-state optical field. Remarkably, the STE emission energy (linewidth) and associated vibrational frequency (linewidth) display Fano resonance versus excitation energy, indicating the many-body quantum interference characteristics of the exciton-phonon hybrid state. Furthermore, we found that the excitation power can modify the excited-state potential and exciton-phonon interaction strength, facilitating the optical tuning of the STE emission and phonon frequency. Our findings reveal the intrinsic exciton-phonon hybrid nature of STEs and establish their optical tuning via a steady-state optical field.

2. Results. The formation dynamics of STE and its dynamic phonon evolution are shown in Fig. 1. First, photoexcitation induces charge transfer from the Ag to In atoms. As shown in the left panel of Fig. 1(a), the free electron-hole pairs are relatively evenly distributed. Owing to the strong exciton-phonon interactions, the excited electrons generate coherent phonon oscillations, especially in the A_{1g} mode, during the first few hundred femtoseconds.[37] The polarization of the A_{1g} mode is depicted in the right panel of Fig. 1(b), showing the atomic displacements with bond lengths in the *ab* plane compressed and those along the *c* axis stretched. Subsequently, the excited electrons are trapped by the lattice deformation potential through reorganization of the excited state structure, yielding the formation of the STE state. At this time, the localized holes are pinned to the Ag atom

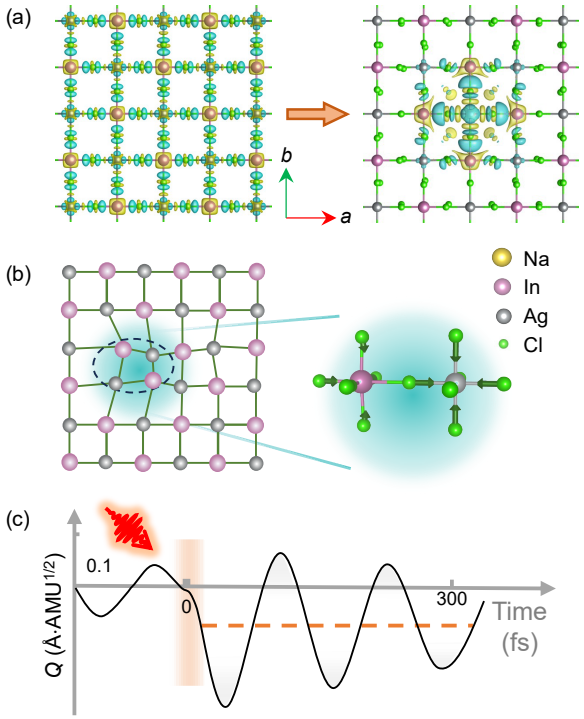

Fig. 1. STE formation and lattice distortion in $Cs_2Ag_{0.4}Na_{0.6}InCl_6$. (a) Differential charge density distribution between the photoexcited and ground states before (left panel) and after (right panel) charge trapping. Yellow and cyan isosurfaces represent the electron and hole orbital densities, respectively. (b) Schematic of lattice and atomic vibration distortion during STE formation; Cl atoms are omitted for clarity. In (a) and (b), the yellow, fuchsia, gray, and green spheres represent Na, In, Ag, and Cl atoms, respectively. (c) Time-resolved atomic displacement (Q) of the A_{1g} phonon mode before and after photoexcitation (black line). Before excitation, Q shows a small-amplitude oscillation about the origin equilibrium position; after photoexcitation, it shows larger-amplitude oscillations about a new equilibrium position (dashed orange line).

sites owing to the large effective mass and screened by the surrounding electrons [right panel of Fig. 1(a)]. Spatial separation arises from the self-trapping of holes in the Ag 4d/Cl 3p orbitals and electrons in the In 5s/Cl 3p orbitals, which, in turn, causes pronounced disparities in the overlap integrals between the electron/hole wave functions and the displacement field of the lattice phonons.[16] Finally, radiative recombination of the STE produces a broad emission spectrum [Fig. 2(a)], and the system returns to its ground state.[38] To examine the transient changes in the A_{1g} mode, we performed time-dependent density functional theory (TDDFT) combined with Ehrenfest molecular dynamics simulations. Figure 1(c) presents the time-resolved atomic displacement (Q) of the A_{1g} mode. Before photoexcitation, the A_{1g} mode vibrates with a small amplitude around the equilibrium position. After photoexcitation [indicated by the orange shadow in Fig. 1(c)], the amplitude increased, shifting to a new equilibrium position (dashed orange line) within a few hundred femtoseconds.[39] The temporal evolution of the A_{1g} phonon amplitude shown in Fig. 1(c) was governed by the displacive excitation of coherent phonons (DECP).[40]

Upon femtosecond laser excitation, the electron redistribution from the valence to the conduction band modifies the interatomic forces, causing an abrupt shift in the equilibrium position of the lattice potential energy surface (PES). According to the Franck-Condon principle, the lattice initially remains at the ground-state position, but subsequently oscillates around the new excited-state equilibrium, producing the observed cosine-like A_{1g} oscillation. The subsequent decay of this coherent vibration is attributed to the lattice anharmonicity, which facilitates the scattering of energy from the A_{1g} mode to other phonon branches. A rigorous mathematical description of this process, including PES expansion and electron-phonon coupling matrix element analysis, is provided in Supplementary Materials Note 9. This lattice distortion aligns with the effect of the localized electron-hole pairs, as shown in the right panel of Fig. 1(a). These results confirm the occurrence of lattice distortion, originating from the localization of excess electrons (i.e., self-trapped electrons). The localized electrons interact strongly with the lattice, displacing atoms from their equilibrium positions and producing the observed distortion. Notably, with resonant excitation, the STE strongly couples with the phonons around the lattice site owing to Fröhlich interaction,[23,41] forming an exciton-phonon hybrid state. The formation of the STE and coherent phonons suggests that adjusting the wavelength and power of the excitation light could be a potential method for tuning the exciton-phonon hybrid state.

$Cs_2Ag_{0.4}Na_{0.6}InCl_6$ exhibits a direct bandgap of 3.71 eV, as confirmed by the Tauc plot of the absorption spectrum [Fig. 2(a)], which is consistent with both the previous report and our computational results.[42] The photoluminescence excitation (PLE) spectrum for the 700 nm emission reveals 355 nm as the near-resonant excitation energy, whereas the 532 nm excitation fails to generate the STE state. The broad emission spectrum with a mean emission wavelength of approximately 608 nm under near-resonant excitation at 355 nm further confirms the formation of STE. Notably, the PLE spectrum deviated from the absorption spectrum (short dotted lines in blue and red), breaking Kasha's rule.[43] This discrepancy stems from variations in the PES of the self-trapped states at different carrier concentrations, leading to excitation-wavelength-dependent emission energy and PLQY [Fig. 3(c)]. These results support the STE origin of broadband emission, excluding defect-related transitions, as shown in Fig. S5. In addition to exciton emission, phonon modes exhibit STE-dependent behavior. To investigate this, we performed polarized Raman spectroscopy using nonresonant 532 nm excitation to observe the phonon modes before STE formation. As shown in Fig. 2(b), two Raman-active phonon modes, A_{1g} and E_g, were identified. Phonon eigenvector diagrams are shown in the inset of Fig. 2(b). Owing to the random distribution of Na^+ (Ag^+) in the lattice, $Cs_2Ag_{0.4}Na_{0.6}InCl_6$ belongs to the O_h group. Combining phonon dispersion from density functional perturbation theory (DFPT), Raman tensors, and polarized Raman spectra, the peaks at approximately 50 and 141 cm^{-1} were identified as E_g vibration modes of

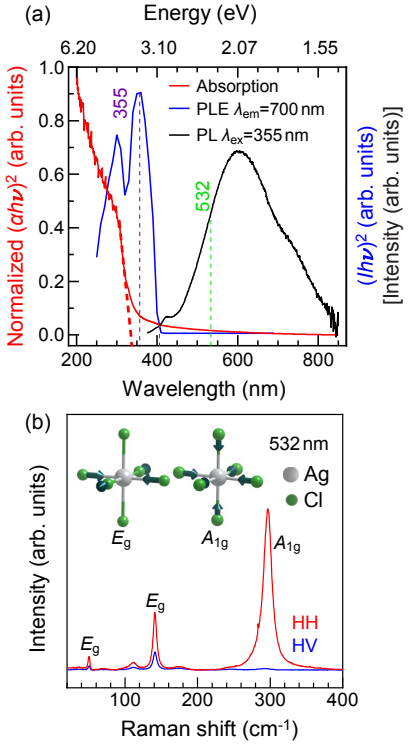

Fig. 2. Optical absorption, exciton emission, and lattice vibration of $Cs_2Ag_{0.4}Na_{0.6}InCl_6$. (a) Absorption, PLE, and PL spectra. The dotted lines indicate two key excitation wavelengths (355 and 532 nm) used in the Raman measurements. The short-dotted line in red (blue) corresponds to the Tauc plot fit of the absorption (PLE) spectrum, yielding a bandgap of 3.71 eV (334 nm). (b) Polarized Raman spectra with 532 nm excitation. The inset shows the vibration of the E_g and A_{1g} modes. The gray and green spheres represent Ag and Cl atoms, respectively. HV and HH represent the cross-polarization and parallel-polarization configurations of incident and scattered light, respectively.

the $(BCl_6)^{5-}$ (B = Ag, In, and Na) octahedrons, with Cl atoms around the B^+ atoms vibrating in various directions. The peak at approximately 296 cm^{-1} is assigned to the A_{1g} mode of the $(BCl_6)^{5-}$ octahedrons, where Cl atoms vibrate in phase. The larger ionic radius of Ag^+ compared to In^+ creates a lattice mismatch, making the Ag-Cl bond stiffer than the In-Cl bond, indicating that the A_{1g} and E_g modes primarily originate from $(AgCl_6)^{5-}$ octahedron vibrations in the perovskite structure. Although the A_{1g} and E_g modes should vanish under the cross (HV) polarization configuration, weak signals were observed, possibly owing to the slight lattice distortion induced by Na cation doping, which relaxed the Raman selection rules.[44]

To examine the effect of STE formation on phonon modes, we performed Raman spectroscopy with excitations below and above the resonant energy. Figure 3(a) presents the Raman spectra obtained with 10 different excitation energies (wavelengths) from 1.58 eV (785 nm) to 4.66 eV (266 nm). A key observation is the mode-selective response under resonant (355 nm) excitation: the A_{1g} mode exhibits a notable redshift, while the E_g mode at approximately 141 cm^{-1} disappears. This contrasting behavior stems from the distinct coupling of each phonon

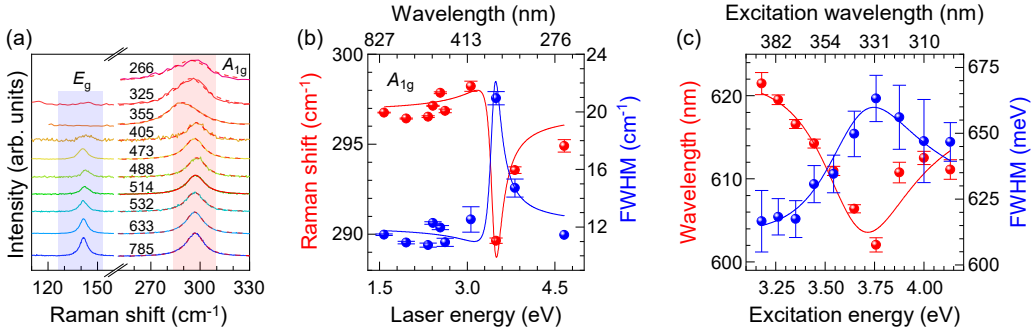

Fig. 3. Renormalization effects of the A_{1g} mode and STE emission in $Cs_2Ag_{0.4}Na_{0.6}InCl_6$. (a) Normalized Raman spectra for 10 excitation wavelengths. (b) Raman shifts and FWHMs of the A_{1g} mode versus excitation energy, extracted from (a). (c) Mean wavelengths and FWHMs of PL spectra versus excitation energy. Solid red and blue curves in (b) and (c) represent Fano function fits, with error bars indicating the fitting uncertainty for Raman shifts and FWHMs.

mode with the STE, which induces a symmetric, breathing-like lattice distortion. This distortion couples strongly to the fully symmetric A_{1g} "breathing" mode, driving its large-amplitude coherent oscillations [as shown in Fig. 1(c)] and softening its frequency [manifested as the redshift in Fig. 3(a)]. However, the force field of the STE couples only weakly with the shear-type displacement pattern of the E_g mode [see the eigenvector in the inset of Fig. 2(b)], providing a negligible driving force for coherent excitation. Furthermore, the disappearance of the E_g mode indicates weak coupling as well as actual lattice instability in the STE state. Our DFPT calculations demonstrated that the frequency of the E_g mode softened significantly and became imaginary at high carrier concentrations, mimicking STE formation (Fig. S7), thereby confirming its dynamic instability. Therefore, under the resonant conditions that generate STEs, the A_{1g} mode emerges as the dominant and stable channel for exciton-phonon coupling, whereas the E_g mode is both weakly coupled and destabilized. Consequently, we focused our subsequent analyses on the A_{1g} mode.

The "soft" lattice and strong exciton-phonon interaction [5,45] promote the formation of an exciton-phonon hybrid state, significantly influencing phonon frequency and damping around the exciton resonance. [25,30] As displayed in Fig. 3(a), the A_{1g} mode experienced significant frequency softening and linewidth broadening near the resonant excitation. The Raman shift and full width at half maximum (FWHM) extracted from Fig. 3(a) follow a Fano line shape [red and blue curves in Fig. 3(b)], indicating many-body quantum interference involving photons, excitons, and phonons. The Fano line shape results from the quantum interference between the discrete (A_{1g} phonon) and continuum (exciton) states, [2,24,25,30,31] where the linewidth of the exciton is considerably larger than that of the phonon. Therefore, the excitation energy can tune the exciton-phonon hybrid state. Under Fano resonance, the phonon frequency $\omega(E_l)$ at excitation energy E_l is denoted by [25,30,31]

$$\omega(E_l) - \omega_0 = \frac{\Delta\omega\left(1 + \frac{E_l - E_{ex}}{q\Gamma}\right)^2}{1 + \left(\frac{E_l - E_{ex}}{\Gamma}\right)^2}, \quad (1)$$

where ω_0 is the bare A_{1g} frequency; E_{ex} and Γ are the energy and damping of the bare free exciton, respectively. $\Delta\omega$ represents phonon frequency softening ($\Delta\omega < 0$) or stiffening ($\Delta\omega > 0$), and the dimensionless parameter q characterizes the relative dipole strength of the renormalized phonon and exciton. The Fano lineshape can describe resonance ($|q| \gg 1$, exciton dominates), anti-resonance ($|q| \ll 1$, phonon dominates), and dispersion ($|q| \approx 1$, comparable phonon and exciton contribution) situations. [30,31] For the A_{1g} frequency, fitting yields $\omega_0 = 298\,\mathrm{cm}^{-1}$, $\Delta\omega = -8\,\mathrm{cm}^{-1}$, $E_{ex} = 3.44\,\mathrm{eV}$, $\Gamma = 0.11\,\mathrm{eV}$, and $q = 2.5$. The q value suggests comparable phonon and exciton contributions, leading to renormalization of the A_{1g} frequency and linewidth. Near the resonant excitation wavelength (355 nm), a pronounced dip appeared, indicating the greatest frequency softening. Because of exciton screening under nonresonant excitation, the A_{1g} frequency was slightly lower than the bare phonon frequency in the ground state. Similarly, the FWHM followed a Fano profile with comparable fitting values [blue curve in Fig. 3(b)], peaking under 355 nm excitation. Without STE formation, the FWHM of the bare A_{1g} mode was approximately $12\,\mathrm{cm}^{-1}$, which increased by approximately $10\,\mathrm{cm}^{-1}$ near resonance.

Because the hybrid state shows half-exciton-half-phonon characteristics, tuning it involves phonon modulation as well as exciton emission manipulation, which is reflected in changes to the PL linewidth and mean wavelength. As shown in Fig. 3(c), both the FWHM and mean wavelength of the PL spectra for the STE [extracted from Fig. S4] followed a Fano line shape. The fitting parameters for the mean wavelength are $\lambda_0 = 622\,\mathrm{nm}$, $\Delta\lambda = -17.5\,\mathrm{nm}$, $E_{ex} = 3.65\,\mathrm{eV}$, $\Gamma = 0.28\,\mathrm{eV}$, and $q = 4.3$, while for the linewidth, the parameters are $\mathrm{FWHM}_0 = 612\,\mathrm{meV}$, $\Delta\mathrm{FWHM} = 42\,\mathrm{meV}$, $E_{ex} = 3.65\,\mathrm{eV}$, $\Gamma = 0.28\,\mathrm{eV}$, and $q = 3$. The agreement of q with the Raman fitting further confirms the exciton-phonon hybrid state, with comparable contributions from both phonons and excitons. Our experimental results demonstrate that optical excitation can efficiently tune both STE emission and phonon modes in this hybrid state.

The exciton–phonon hybrid state can be adjusted by varying the exciton concentration, altering the exciton–phonon interaction and lattice distortion, leading to

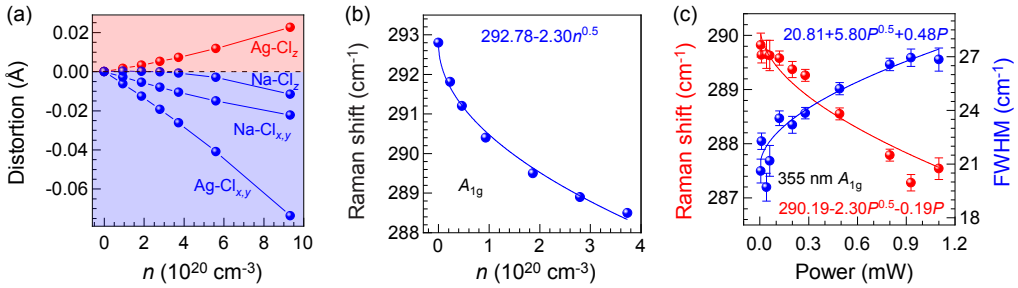

Fig. 4. Calculated variation of bond length and A_{1g} frequency, together with excitation power-dependent frequency and FWHM of the A_{1g} mode. (a) Distortion of bond length for Ag-Cl$_{x,y}$, Ag-Cl$_z$, Na-Cl$_{x,y}$, and Na-Cl$_z$ versus carrier concentration n. (b) Calculated A_{1g} frequency versus carrier concentration. (c) Raman shifts and FWHMs of the A_{1g} mode with increasing excitation power at 355 nm excitation. Error bars represent fitting uncertainty for Raman shifts and FWHMs. Solid red and blue curves in (b) and (c) show the fitting results.

phonon self-energy renormalization[46] and changes in the phonon frequency and damping.[20] As shown in Fig. S2, we evaluated the exciton-phonon interaction strength by calculating the excited state potential, which is indicative of the Huang-Rhys factor (S^* factor), with increasing carrier concentration n. The S^* factor increased with n^2, indicating enhanced exciton-phonon interactions at higher carrier concentrations. To evaluate the effect of the carrier concentration on the lattice distortion, we calculated the variations in the bond lengths of Ag-Cl$_{x,y}$, Ag-Cl$_z$, Na-Cl$_{x,y}$, and Na-Cl$_z$. As shown in Fig. 4(a), Ag-Cl bonds vary, with only the Ag-Cl$_z$ bond stretching as n increased. Because the dominant lattice distortion direction aligns with the vibrational direction of the Raman-active A_{1g} mode, this results in an apparent frequency softening of the A_{1g} mode when forming the STE state. To understand this softening intuitively, we calculated the A_{1g} frequency as a function of n using the constrained density functional theory (CDFT) method, as shown in Fig. 4(b). The frequency decreases with increasing n, satisfying $\omega_c = 292.78 - 2.30n^{0.5}$. This $n^{0.5}$ dependence is similar to that of the plasma frequency with screening effects (proportional to $n_e^{0.5}$). For a small q, in the Thomas-Fermi approximation, the oscillation frequency is denoted by[47]

$$\omega(q) = \sqrt{\frac{4\pi Z e^2 n_e}{M k_{TF}^2}}\, q, \tag{2}$$

where Z is the number of electrons per primitive unit cell, n_e is the electron density, M is the ion mass, k_{TF}^2 is the Thomas–Fermi wave number, and q is the wave vector. The similar $n^{0.5}$ dependence indicates that, like electrons shielding ions, phonons "dressed" by the exciton cloud experience excitonic shielding, highlighting their comparable contributions within the exciton-phonon hybrid state. Because the excitation power (P) is directly proportional to the carrier concentration (n), we performed power-dependent Raman spectra measurements under near-resonant 355 nm excitation to further investigate the carrier concentration effect. As shown in Fig. 4(c), a pronounced decrease in frequency and an increase in FWHM of the A_{1g} mode can be observed with increasing excitation power. In addition to the carrier concentration effect, the sample heating effect, causing a linear redshift in frequency with increasing temperature, should be considered.[48] Considering the linear relation between sample temperature and absorbed excitation power within our experimental power range,[49,50] the Raman shift and FWHM can be fitted using $\omega = 290.19 - 2.30P^{0.5} - 0.19P$ and FWHM $= 20.81 + 5.80P^{0.5} + 0.48P$, respectively, accounting for both the carrier concentration effects ($P^{0.5}$ dependence) and sample heating effects (P dependence). The carrier concentration effect coefficient matches well with the theoretical result [Fig. 4(b)], and the ratio of sample heating to the carrier concentration effect is 8.3%, indicating that the observed Raman frequency softening under 355 nm excitation is typically owing to the enhanced exciton-phonon interaction rather than the laser-induced heating effect. By contrast, under 532 nm excitation, both the Raman shift and FWHM remained nearly unchanged with increasing power. The full power-dependent spectra under 532 and 355 nm excitation are shown in Fig. S8. Our results demonstrate that all-optical methods, including varying the excitation energy and power, can manipulate the hybrid state by adjusting the carrier concentration and exciton-phonon interactions.

3. Discussions. Using near-resonant Raman and PL spectroscopy techniques, we experimentally demonstrated the existence and manipulation of the exciton-phonon hybrid state in the double-halide perovskite $Cs_2Ag_{0.4}Na_{0.6}InCl_6$. The hybrid nature is revealed through the Fano line shape in the phonon and STE emissions versus the excitation energy. DFT calculations show that the A_{1g} phonon mode dominates STE formation, with phonon softening attributed to the increasing carrier concentration and enhanced exciton-phonon interactions. The quantum interference between excitons and phonons is strongly influenced by phonon vibrations, excitation energy, and excitation power, allowing the tuning of the hybrid state. This tunable coupling between STEs, phonon vibrations, and external light fields presents a promising platform for investigating exciton-phonon interactions in strongly coupled systems. The underlying mechanism is governed by material descriptors, such as exciton localization, orbital mismatch (yielding a large $|D_e - D_h|$), and soft optical phonons and can guide the search for candidate families, including low-dimensional perovskites and charge-transfer insulators. Moreover, the steady-state optical method used to explore multibody quantum interference can be extended to other systems. Our findings will

facilitate the development of optically modulated STE-based devices.

Materials and Methods.

Materials Synthesis. High-quality centimeter-sized bulk single crystals of $Cs_2Ag_{0.4}Na_{0.6}InCl_6$ doped with 0.04% bismuth (Bi^{3+}) doping were synthesized using a hydrothermal method. Further details regarding sample preparation are provided in previous studies.[16] The crystal structure was characterized by X-Ray diffraction (see Ref. [51] for full data), which confirmed the (111) orientation of the cleaved surface and yielded a lattice constant of $a = 10.518$ Å, consistent with a high-quality single crystal. In this study, the Bi^{3+} doping concentration was maintained at a low level (0.04%) to suppress the characteristic emission behavior. At such a low concentration, Bi^{3+} typically acts as a defect passivator and exciton localization promoter rather than contributing to the emission spectrum. This ensures that the intrinsic photophysical properties of the host material remain dominant, while benefiting from the improved crystal quality and reduced nonradiative recombination induced by Bi^{3+} doping (enhancing PLQY).

Material Characterization. The absorption spectra were measured using a UV-Vis spectrophotometer. The PL spectra under excitation at 355 nm and the contour plot of the PLE spectra were obtained using an Edinburgh FLS-1000 fluorescence spectrophotometer. For the PLE measurements, we employed a continuous-wave (CW) xenon lamp (0.37 mW) coupled with a monochromator as the excitation source. The power-dependent PL spectra under 360 nm excitation (maximum power of 1 mW) at 4 K were measured using the LabRam HR Evolution (100 gr/mm grating) and attoDRY 800 systems. PL lifetime measurements were performed using time-correlated single-photon counter technology. A pulsed 375 nm diode laser with a 50 ps pulse and a repetition rate of 16 MHz was used as the excitation source.

Ten different CW lasers were employed in the Raman measurements, and the maximum laser powers were selected to avoid sample damage: 266 nm (all-solid-state CW UV laser, 0.152 mW), 325 nm (He-Cd laser, 0.936 mW), 355 nm (diode-pumped solid-state laser, 1.1 mW), 405 nm (narrow linewidth diode laser, 0.035 mW), 473 nm (diode-pumped solid-state laser, 14.5 mW), 488 nm (tunable argon-ion laser, 4.2 mW), 514 nm (tunable argon-ion laser, 4.2 mW), 532 nm (single-frequency diode-pumped laser, 37.5 mW), 633 nm (He-Ne laser, 7.8 mW), and 785 nm (narrow linewidth diode laser, 20.3 mW). The Raman spectra under 266, 325, 473, 532, 633, and 785 nm excitations were measured using a LabRam HR Evolution system equipped with a liquid nitrogen-cooled charge-coupled device (CCD) detector, whereas those under 355, 405, 488, and 514 nm excitations were measured using a T64000 system. A 100× objective lens (numerical aperture NA = 0.90) was employed to collect signals under visible light excitation, whereas a 15× objective lens (NA = 0.32) was used for ultraviolet excitation. Raman measurements were performed using 1800 gr/mm grating.

First-Principles Calculations. All first-principles DFPT calculations were performed using the projector augmented wave method, as implemented in the Vienna Ab initio Simulation Package with the PAW potentials. We adopted the PBE0 hybrid functional, which can correct self-interaction errors in the generalized gradient approximation (GGA), to describe the exchange-correlation interactions. To simulate the effect of Na-atom doping, we chose a half-substituted structure $Cs_2Ag_{0.5}Na_{0.5}InCl_6$, as shown in Fig. 1(b), where Ag atoms alternate with Na atoms to form a layered structure. According to our tests, the fully relaxed structure obtained using the Perdew–Burke–Ernzerhof (PBE) functional underestimated the frequency of the A_{1g} mode by approximately 10.4%. Therefore, the phonon structures were calculated using the PBEsol functional, which were in excellent agreement with the experimental results.[52] We obtained the lattice parameters $a = b = 21.18$ Å and $c = 10.662$ Å. The plane-wave energy cutoff was set to 800 eV, and the atomic forces were converged to within 10^{-5} Ry/a.u. CDFT was employed to calculate the softening of the A_{1g} mode and PES as implemented in the Quantum Espresso package, which accurately describes the phonon frequency under laser illumination[52] and the electron-phonon coupling.[53] The methodology for calculating the time-resolved atomic displacement amplitude (Q) of the A_{1g} mode using TDDFT combined with Ehrenfest molecular dynamics simulations has been described in detail in the previous article.[54]

TDDFT simulations in this study were performed using the in-house software package TDAP. Electron–ion interactions were treated within the norm-conserving pseudopotential formalism to reduce the computational cost. The pseudopotentials for each angular momentum channel (l) were generated using the Troullier-Martins parameterization. Electron–electron interactions were described using the PBE exchange–correlation functional. Owing to computational constraints, the $Ag_{0.5}Na_{0.5}$ doping configuration was modeled using a single unit cell with lattice parameters $a = b = 10.484$ Å and $c = 10.477$ Å together with Γ-point-only Brillouin-zone sampling. All atomic coordinates and lattice parameters were fully relaxed, with residual Hellmann–Feynman forces on each atom below 0.001 eV/Å.

The projection of the phonon amplitudes in Fig. 1(c) is based on the principle that atomic displacements within a unit cell from their equilibrium positions can be expressed as a linear combination of the phonon normal coordinates, as follows:

$$\boldsymbol{u}_l(s) = \frac{1}{\sqrt{NM_s}} \sum \boldsymbol{e}_{k,\sigma}(s) Q_{k\sigma} \mathrm{e}^{\mathrm{i}\boldsymbol{k}\cdot\boldsymbol{R}_l}.$$

Here, $\boldsymbol{u}_l(s)$ denotes the displacement vector of atom s in the l-th unit cell relative to its equilibrium position; N is the number of unit cells in the selected computational cell; M_s is the relative atomic mass of atom s; $\boldsymbol{e}_{k,\sigma}(s)$ is the phonon eigenvector polarization vector of branch σ at wavevector $\boldsymbol{k}$; and $Q_{k\sigma}$ is the phonon normal coordinate, corresponding to the phonon amplitude plotted in Fig. 1(c). The phonon eigenvectors $\boldsymbol{e}_{k,\sigma}(s)$ were obtained using DFPT. The phonon normal coordinates were extracted by projection using the orthonormality condition,

$\sum_s \boldsymbol{e}^*_{k\sigma}(s) \cdot \boldsymbol{e}_{k\sigma'}(s) = \delta_{\sigma\sigma'}$, where $\delta_{\sigma\sigma'}$ is the Kronecker delta.

The self-trapped state was calculated as follows: First, the atomic configuration of the self-trapped state was identified. By manually imposing a population inversion and subsequently relaxing the atomic structure, we obtained a localized atomic configuration corresponding to the excited state. Based on this relaxed atomic structure, the ground-state PES could be evaluated along different normal-mode coordinates, as illustrated by the blue curve connecting the data points in Fig. S2(b). The excited-state PES along the same normal-mode coordinates was computed analogously by enforcing a population inversion. The self-trapping energy is defined as the difference between the excited-state energy at the equilibrium geometry and that at the self-trapped atomic structure. This quantity represents the energy reduction in the excited state emerging from electronic localization and the accompanying lattice distortion.

The chosen methodology, particularly the supercell size, corresponds to a specific carrier concentration that can influence the estimated exciton-phonon coupling strength. Although the finite supercell size (160 atoms) prevented reaching the strict dilution limit, CDFT analysis confirms that our results accurately capture the qualitative physical trends of the self-trapping process. As detailed in Supplementary Materials Note 2 and Fig. S2, the calculations indicate that increasing carrier concentration enhances lattice distortion and the resulting coupling strength.

Note. J. Z., S. M., and S. G. conceived the project. J. L. and J. T. provided samples. K. X. and S. P. performed the experiments with the support of Z. Z., Y. W., and H. C. X. L. performed the simulations. J. Z., S. M., and S. G. supervised this study. All authors discussed the results and revised the manuscript. The authors declare no conflict of interest.

Acknowledgments. J. Z. acknowledges funding support from the National Natural Science Foundation of China (Grant No. 12525405) and the CAS Project for Young Scientists in Basic Research (Grant No. YSBR-120). S. G. acknowledges funding support from the National Natural Science Foundation of China (Grant No. 12393831). The authors thank Prof. Minghui Fan at the USTC for her valuable support in conducting the Raman measurements as part of the Grand Technical Talent Promotion Plan (Grant No. TS2021002).

References

[1] Ziman J M 2001 *Electrons and Phonons: The Theory of Transport Phenomena in Solids* (Oxford: Oxford University Press)
[2] Feliciano G 2017 *Rev. Mod. Phys.* **89** 015003
[3] Lanzara A, Bogdanov P V, Zhou X J, Kellar S A, Feng D L, Lu E D, Yoshida T, Eisaki H, Fujimori A, Kishio K, Shimoyama J I, Noda T, Uchida S, Hussain Z, and Shen Z X 2001 *Nature* **412** 510
[4] Peter Y U and Cardona M 2010 *Fundamentals of Semiconductors: Physics and Materials Properties* (Berlin: Springer Science & Business Media)
[5] Franchini C, Reticcioli M, Setvin M, and Diebold U 2021 *Nat. Rev. Mater.* **6** 560
[6] Williams R T and Song K S 1990 *J. Phys. Chem. Solids* **51** 679
[7] Puppin M, Polishchuk S, Colonna N, Crepaldi A, Dirin D N, Nazarenko O, De Gennaro R, Gatti G, Roth S, Barillot T, Poletto L, Xian R P, Rettig L, Wolf M, Ernstorfer R, Kovalenko M V, Marzari N, Grioni M, and Chergui M 2020 *Phys. Rev. Lett.* **124** 206402
[8] Yue X, Wang C, Zhang B, Zhang Z, Xiong Z, Zu X, Liu Z, Hu Z, Odunmbaku G O, Zheng Y, Sun K, and Du J 2023 *Nat. Commun.* **14** 917
[9] Dyksik M, Beret D, Baranowski M, Duim H, Moyano S, Posmyk K, Mlayah A, Adjokatse S, Maude D K, Loi M A, Puech P, and Plochocka P 2024 *Adv. Sci.* **11** e2305182
[10] David E 2013 *Polarons* (Cambridge: Cambridge University Press)
[11] Félix T, Valverde-Chávez D A, Quarti C, Cortecchia D, Bargigia I, Beljonne D, Petrozza A, Silva C, and Srimath Kandada A R 2019 *Nat. Mater.* **18** 349
[12] Zhou R, Sui L, Liu X, Liu K, Guo D, Zhao W, Song S, Lv C, Chen S, and Jiang T 2023 *Nat. Commun.* **14** 1310
[13] Toyozawa Y 1961 *Prog. Theor. Phys.* **26** 29
[14] Dai Z, Lian C, Lafuente-Bartolome J, and Giustino F 2024 *Phys. Rev. Lett.* **132** 036902
[15] Liu H, Wang A, Zhang P, Ma C, Chen C, Liu Z, Zhang Y Q, Feng B, Cheng P, and Zhao J 2023 *Nat. Commun.* **14** 3690
[16] Luo J, Wang X, Li S, Liu J, Guo Y, Niu G, Li Y, Fu Y, Gao L, Dong Q, Zhao C, Leng M, Ma F, Liang W, Wang L, Jin S, Han J, Zhang L, Etheridge J, and Wang J 2018 *Nature* **563** 541
[17] Chang T, Kou T T, Wei Q L, Li X, Han X X, Wang L, Han S G, and Yu W W 2025 *ACS Photonics* **12** 5231
[18] Zeng P, Wang F, Zhang Y, Zhou W, Guo Z, Wu X, Lu M, and Zhang S 2021 *ACS Photonics* **8** 1353
[19] Suo H, Wang N, Zhang Y, Zhang X, Xiang J, Wang X, Xing G, Guo D, Chang J, and Wang Y 2025 *Light Sci. Appl.* **14** 21
[20] Lanigan-Atkins T, He X, Krogstad M J, Pajerowski D M, Abernathy D L, Xu G N M N, Xu Z, Chung D Y, Kanatzidis M G, Rosenkranz S, Osborn R, and Delaire O 2021 *Nat. Mater.* **20** 977
[21] Li X, Wang A, Chen H, Tao W, Chen Z, Zhang C, Li Y, Zhang Y, Shang H, and Weng Y X 2022 *Nano Lett.* **22** 8755
[22] Yazdani N, Bodnarchuk M I, Federica B, Norberto M, Ina F, Burak G, Benjamin L C, Marc Z, Gabriele R, Maximilian J, Simon C B, Maksym Y, Lin M F, Michael K, Alexander R, Shen X, Stephen W, Wang X, Eric V, Antonietta G 2024 *Nat. Phys.* **20** 47
[23] Steele J A, Puech P, Keshavarz M, Yang R, Banerjee S, Debroye E, Kim C W, Yuan H, Heo N H, Vanacken J, Walsh A, Hofkens J, and Roeffaers M B J 2018 *ACS Nano* **12** 8081
[24] Thomas P D and Rudi H 2007 *Rev. Mod. Phys.* **79** 175
[25] Fano U 1961 *Phys. Rev.* **124** 1866
[26] Miroshnichenko A E, Flach S, and Kivshar Y S 2010 *Rev. Mod. Phys.* **82** 2257
[27] Luk'yanchuk B, Zheludev N I, Maier S A, Halas N J, Nordlander P, Giessen H, and Chong C T 2010 *Nat. Mater.* **9** 707
[28] Limonov M F, Rybin M V, Poddubny A N, and Kivshar Y S 2017 *Nat. Photonics* **11** 543
[29] Rousseau D L and Porto S P S 1968 *Phys. Rev. Lett.* **20** 1354
[30] Tang T T, Zhang Y B, Park C H, Geng B, Girit C, Zhao H, Michael C M, Alex Z, Crommie M F, Louie S G, Shen Y R, and Wang F 2009 *Nat. Nanotechnol.* **5** 32
[31] Tan Q H, Li Y M, Lai J M, Sun Y J, Zhang Z, Song F, Robert C, Marie X, Gao W, Tan P H, and Zhang J 2023 *Nat. Commun.* **14** 88

[32] Yan F, Xing J, Xing G, Quan L, Swee T T, Zhao J X, Su R, Zhang L L, Chen S, Zhao Y W, Huan A, Edward H S, Xiong Q H, and Demir H V 2018 *Nano Lett.* **18** 3157

[33] Xiang H, Wang R, Chen J, Li F, and Zeng H 2021 *Light Sci. Appl.* **10** 206

[34] Li J, Wang J, Ma J, Shen H, Li L, Duan X, and Li D 2019 *Nat. Commun.* **10** 806

[35] Yang H, Lu H, Wang X, Sun W, Yang Y, Wei X, Long G, Xu J, Zhang X, and Yuan M 2025 *Light Sci. Appl.* **14** 297

[36] Song S Y, Gao C J, Zhou R, Wang B Z, Zhao W B, Cao Q, Hu Y W, Dong L, Liu K K, and Shan C X 2025 *Light Sci. Appl.* **14** 249

[37] Wang C, Liu X, Chen Q, Chen D, Wang Y, and Meng S 2023 *Phys. Rev. Lett.* **131** 066401

[38] Li S, Luo J, Liu J, and Tang J 2019 *J. Phys. Chem. Lett.* **10** 1999

[39] Dexheimer S L, Van Pelt A D, Brozik J A, and Swanson B I 2000 *Phys. Rev. Lett.* **84** 4425

[40] Zeiger H, Vidal J, Cheng T, Ippen E, Dresselhaus G, and Dresselhaus M 1992 *Phys. Rev. B* **45** 768

[41] Chen B, Chen R, and Huang B 2023 *Adv. Energy Sus. Res.* **4** 2300018

[42] Peng K, Yu L, Min X, Hu M, Yang Y, Huang S, Zhao Y, Deng Y, and Zhang M 2022 *J. Alloys Compd.* **891** 161978

[43] Lewis G N and Kasha M 1944 *J. Am. Chem. Soc.* **66** 2100

[44] Siddique H, Xu Z, Li X, Saeed S, Liang W, Wang X, Gao C, Dai R, Wang Z and Zhang Z 2020 *J. Phys. Chem. Lett.* **11** 9572

[45] Tan J, Li D, Zhu J, Han N, Gong Y, and Zhang Y 2022 *Nanoscale* **14** 16394

[46] Lafuente-Bartolome J, Lian C, Sio W H, Gurtubay I G, Eiguren A, and Giustino F 2022 *Phys. Rev. Lett.* **129** 076402

[47] Czycholl G 2023 *Solid State Theory* (Springer Berlin, Heidelberg)

[48] Xu K X, Lai J M, Gao Y F, Song F, Sun Y J, Tan P H, and Zhang J 2022 *Phys. Rev. B* **106** 085205

[49] Chen Y, Peng B, Cong C, Shang J, Wu L, Yang W, Zhou J, Yu P, Zhang H, and Wang Y 2019 *Adv. Mater.* **31** 1804979

[50] Easy E, Gao Y, Wang Y, Yan D, Goushehgir S M, Yang E H, Xu B, and Zhang X 2021 *ACS Appl. Mater. Interfaces* **13** 13063

[51] Pang S, Liu X, Luo J, Xie Y, Tang J, Meng S, Tan P H, and Zhang J 2022 *Adv. Photonics Res.* **3** 2100222

[52] John P P, Adrienn R, Gábor I C, Oleg A V, Gustavo E S, Lucian A C, Zhou X, and Burke K 2008 *Phys. Rev. Lett.* **100** 136406

[53] Marini G, and Calandra M 2021 *Phys. Rev. Lett.* **127** 257401

[54] Liu X B, Hu S Q, Chen D, Guan M, Chen Q, and Meng S 2022 *Nano Lett.* **22** 4800